www.czasopisma.pan.pl PAN POLSKA AKADEMIA NAUK www.journals.pan.pl

Arch. Metall. Mater. **67** (2022), 3, 843-853

DOI: https://doi.org/10.24425/amm.2022.139674

HARUN GÖKÇE[1*]

EXPERIMENTAL AND NUMERICAL INVESTIGATION OF CUTTING FORCES AND TEMPERATURES IN MILLING OF CUSTOM 450 STEEL

Stainless steels have a wide usage field, their needs as structural parts are increasing day by day due to their resistance to corrosion and providing sufficient mechanical strength in environments that would cause corrosion. In addition to high mechanical properties of the stainless steels, the low heat transmission coefficients bring problems during machining. In this study, the suitable cutting tool and cutting parameters have been evaluated in terms of cutting forces and the tool temperature, the experimental results and finite element analysis have been compared in the milling of Custom 450 stainless steel which offers especially an excellent working opportunity at high temperature and salinity environment. Milling experiments have been carried out using L16 experimental design for Taguchi method. Four simulations have been made using finite element method with corresponding values in L16 orthogonal array for optimum cutting tool and the results were compared in terms of cutting forces and tool temperature changes.

Keywords: End milling; Finite element method; Custom 450; Cutting force; Cutting temperature

1. Introduction

Thanks to their unique corrosion resistance, low thermal conductivity and delivering high mechanical properties, stainless steels are used in particularly medical, food, chemical industries, including marine and nuclear power plants and their needs continue to increase every day [1,2]. Custom 450 is a martensitic stainless steel grade, which offers corrosion resistance up to 650°C and its mechanical properties can be increased significantly by heat treatment methods. It is highly resistant to pitting and corrosion in liquid environments with a salt content of 20% [3]. Although there are many publications made on many stainless steel types, studies made on Custom 450 are relatively limited.

Exhibiting high mechanical characteristics and low heat conduction affects negatively forming of stainless steel by machining [4,5]. Different types of stainless steels also affect the mechanical properties and can significantly change the machinability [6,7]. The high loads generated during cutting and the resulting heat causes rapid wear of the cutting tool and consequently deviations from surface roughness and geometric tolerances do occur [8,9]. In addition, the feedrate, cutting depth and insert radius influence the roughness values [10,11]. While the shear forces increase with increasing feedrate, a small amount of decrease in forces is observed with increased cutting speed [12,13]. It has a significant effect on the machinability of the cutting tool during the cutting process. Variables such as tool geometry, material, coating type and thickness change the machining efficiency of stainless steel [14].

Gokce et al., examined the effects of tool coating, cutting speed and workpiece material on cutting forces and surface roughness in shoulder milling of commercial pure molybdenum materials. He stated that the type of coating was effective on cutting forces [15]. Basmaci, examined the cutting forces and surface roughness in turning of 17-4 PH stainless steel in terms of feedrate, depth of cut and the tool radius. They stated that the best results were obtained with coated carbide tools [16]. Selaimia et al., examined the milling of X2CrNi18-9 austenitic stainless steels in dry conditions by means of coated carbide tools in different cutting parameters in terms of surface roughness, cutting force, cutting power, specific cutting force and depth of cutting rate. They stated that feedrate was effective on surface roughness and on specific cutting force and the cutting power were affected by the depth of cutting [17].

Varghese et al., used coated carbide cutting tools to examine tool wear performance during dry milling of AISI 304 stainless steel, and at the end of the experiment they found out that the coating on the tools was removed and micro cracks were

[1] INDUSTRIAL DESIGN ENGINEERING DEPARTMENT IN GAZI UNIVERSITY, ANKARA, TURKEY

* Corresponding authorl: harungokce@yahoo.ca

formed [18]. Kuram et al., subjected AISI 304 stainless steel material to micro milling experiments with spherical tipped cutting tools. They studied the effects of spindle speed, feedrate and depth of cutting on tool wear, cutting forces and surface roughness using regression and fuzzy logic methods. The results showed that fuzzy logic as well as the regression modelling methods could be used efficiently to predict tool wear, cutting forces and surface roughness [19].

Lin, optimized three cutting parameters such as cutting speed, feedrate and depth of cutting during shaping of stainless steel material by milling method by taking into account multi performance characteristics such as chip volume, surface roughness and chip height [20]. Lin, in another study of his, examined the burr formation and tool wear during milling of stainless steels. He stated that the burr height depended on the milling type and that changes in cutting parameters could produce different forms of burrs at the exit edge [21].

Nordin et al. studied tool wear caused by milling austenitic stainless steel with multi- and single-layer coated carbide tools. They observed mechanical and chemical wear mechanisms and stated that crack formation is the most effective wear on tool life. They emphasized that multilayer coatings consisting of TiN and TaN are suitable for milling austenitic stainless steel [22]. Qashim et al., examined the lateral milling process for AISI 304 stainless steel. Using grey fuzzy logic, they optimized spindle speed, feedrate, axial cutting depth and radial cutting depth in terms of tool life and chip formation [23]. Maurel Pantel et al., used Lagrangian formulation and Johnson-Cook (JC) parameters to simulate lateral milling operations on AISI 304L stainless steel. They performed lateral milling experiments to examine the machinability of this material and to validate the results obtained from the 3D finite element model developed [24].

In this study, the appropriate cutting tool and cutting parameters in the milling of Custom 450 stainless steel were evaluated in terms of cutting forces and tool temperature, and the results of the experimental study were compared with the finite element method. For the Taguchi method, milling experiments were carried out using the L16 experimental design. ANOVA was performed to determine the significance levels of the cut-off parameters on the measured values. For the optimum cutting tool, four simulations were made using the finite element method with corresponding values in the L16 orthogonal array and the results were compared in terms of cutting force and temperature change.

2. Materials Method

2.1. Used equipment and cutting conditions

Milling experiments were performed at an Arion IMM-600 CNC vertical machining center. The heat formed during the processing was measured with a Fluke Ti200 thermal imaging camera. Cutting forces were measured with a Kistler 9257B dynamometer. The cutting tool temperature was determined by measuring the highest temperature value measured on the cutting tool with a thermal camera. The resultant force (R), in which the F_x, F_y and F_z components are evaluated together, is based on the shear force Eq. (1). The measurements for the three cutting force components (F_x, F_y and F_z) are the average values taken from the stable region of the graphs taken from the dynamometer (the parts of the cutting tool entering and exiting the material are not included in the calculations since it is an unstable region). Custom 450 stainless steel material was shaped into 60×60×8 mm. The chemical composition and some properties of the workpiece are given in TABLE 1.

$$R = \sqrt{F_x^2 + F_y^2 + F_z^2} \tag{1}$$

TABLE 1

Mechanical properties of Custom 450 H900 [25]

Properties	Unit	
Chemical components	%	C < 0.05, 14-16Cr, 1.25-1.75Cu, 75Fe, Mn < 1, 0.5-1Mo, 5-7Ni,
Density	g/cm^3	7.75
Hardness	birinell	278
Yield	MPa	814
Shrink	MPa	979
Elasticity	GPa	200
Poisson		0.29
Heat Cond.	W/m-K	15

Cutting tools were decided on by user recommendations and literature research and obtained from different manufacturers. Cutting tools with an insert radius of 0.4 mm were mechanically connected to a single tool holder, Ø12 mm in diameter. The cutting tool and tool holder characteristics are given in TABLE 2. Cutting tests were performed using face milling method in dry cutting conditions. The cutting tool was centered on the 8 mm (radial cutting depth) face of the workpiece and positioned to have an axial cutting depth of 2 mm.

TABLE 2

Characteristics of cutting tools and holders [1]

No	Customer	Insert and tool holder code	Grade
1	Kenna metal	EDPT10T304PDSRG 12A01R020A16ED1	KC522M PVD (Al,Ti)N
2	Mitsu bishi	AOMT123604PEER KMTAOMT100R 121W16S	VP15TF PVD (Al,Ti)N
3	Sandvik	R390-11 T308M R390-012A16-11L Coromill 390	PM 4240 CVD Ti(C,N) + Al_2O_3 + TiN)
4	Sandvik	R390-11 T308M R390-012A16-11L Coromill 390	H13A Uncoated

2.2. Experimental setup

In this study, cutting tool temperature and cutting forces during shaping of Custom 450 stainless steel material by milling was examined using Taguchi method. Cutting speed (V_c)

and feedrate (f) of the Cutting tool (CT) were determined as control factors and 4 levels were selected for each control factor. The temperature values formed on the CT were determined as quality characteristics. The L16 vertical sequence was used as the experimental design for the taguchi method. Control factors and levels are given in TABLE 3.

TABLE 3

Control factors and levels [1]

Factors	Unit	Code	Levels			
			1	2	3	4
Cutting Tool (CT)	—	A	T1	T2	T3	T4
Cutting Speed (V_c)	m/min.	B	40	80	120	160
Feedrate (f)	mm/rev	C	0.05	0.10	0.15	0.20

In order to determine the appropriate levels of control factor, the case where the quality characteristic values are smallest should be determined. For this purpose, Signal/Noise (S/N) ratio was calculated using the "smallest best" objective function Eq. (2). To determine the effects of control factors on quality characteristics, ANOVA was applied for 95% confidence interval of the experimental results. These operations were performed on Minitab 17 software.

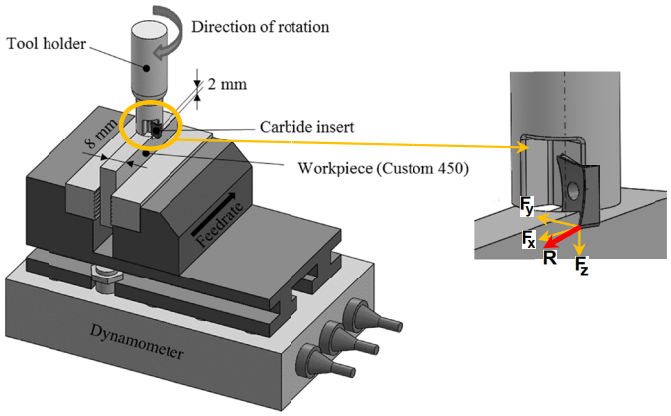

Fig. 1. 3D CAD model of test setup

$$S/N = -10\log\left(\frac{1}{n}\sum_{i=1}^{n} y_i^2\right) \tag{2}$$

2.3. Cutting tool design

In the study, the model information of the CT was obtained with the help of a 3D scanner. The scanner used to scan CT's can be adjusted to five different resolutions ranging from 0.4 to 5.0 megapixels, operating with miniature projection technique, with a 5 MP camera in a large field of view of 1500 mm. Scanning is performed on an AICON Smart r5 scanner.

Point cloud data imported into CATIA V5 software was converted to Stereolithographic (STL) format. The number of points obtained on the CT is 10542. A mesh model was created between the points to make remodeling over the point cloud. The

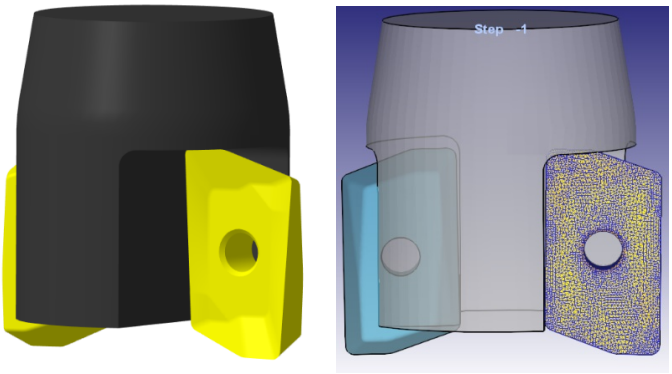

Fig. 2. 3D CT CAD and finite element model

mesh structure was prepared with the largest mesh size being 1 mm and the maximum distance of 0.1 mm between points. The mesh model is divided into zones based on the skewness and radius transformations considering the distance changes of the points.

With the definition of zones, the separation of plane and cylindrical structures on the workpiece was made possible. By making use of these form structures, a planar surface was formed on the side surface and the middle of the workpiece.

It is very important to minimize the deviation between the resulting 3D CT model and point cloud data. For this, it is necessary to perform a deviation analysis for all surfaces obtained by zone definitions. Deviation analysis is examined by taking into consideration the variables of dimensions of workpiece, working accuracy and regional stability. The maximum permissible deviation for these CTs is 0.02 mm. For this reason, the analysis control was performed on each surface. Fig. 2 illustrates the 3D CT model and the mesh pattern obtained via reverse engineering. In order to perform Finite Element Analysis (FEA) in machining process, it is necessary to enter the properties of the workpiece material correctly and a life-sized CT must be designed. For this reason, the workpiece material properties in the FEA model were obtained by reference to the library of DEFORM-3D software.

2.4. Workpiece

One of the most important elements for an accurate FEA in machining is the correct entry of workpiece material properties and the life-sized design of the CT. Therefore, it is important to determine the plastic deformation properties in addition to the elastic properties of the workpiece material in the FEA model. As the chip removal phenomena involves the plastic deformation and separation structure of a material, the properties of the material that were determined with this purpose through empirical studies must be introduced to the FEA. The JC material model is used for these purposes.

$$\bar{\sigma} = \left[A \times B\left(\left(\bar{\varepsilon}^{pl}\right)\right)^{n}\right]\left[1 + C\ln\left(\frac{\dot{\varepsilon}^{pl}}{\varepsilon_0}\right)\right]\left[1 - \theta^{m}\right] \tag{3}$$

$$\theta = \begin{pmatrix} 0 & \text{for} & T < T_\varphi \\ \left(\dfrac{T - T_0}{T_m - T_0}\right) & \text{for} & T_0 < T < T_m \\ 1 & \text{for} & T \geq T_m \end{pmatrix} \tag{4}$$

The *JC* plasticity model is a particular type of von Mises plasticity model, which includes analytical forms and adherence to the hardening law; is suitable for the deformation of the high tension ratio of many materials, including most metals; and is typically used in adiabatic transient dynamic simulations. Yield stress is given in Eq. (3) [26].

Where: A is yield stress at ambient temperature, B hardening module, n stress hardening exponent, C stress ration constant, $\overline{\varepsilon}^{pl}$ plastic stress, ε^{pl} plastic stress ratio, ε_o reference stress ratio, T current temperature, T_m melting temperature, T_o reference temperature and the room temperature value. The *JC* dynamic deformation model is based on the equivalent plastic stress value at the element integration points; deformation is assumed when the damage parameter exceeds 1. D damage parameter is presented in Eq. (5) [27].

$$D = \sum \frac{\Delta \overline{\varepsilon}^{pl}}{\overline{\varepsilon}_f^{pl}} \tag{5}$$

When there is an increase in equivalent plastic stress $\overline{\varepsilon}^{pl}$, all increases in the analysis are summed. $\overline{\varepsilon}_f{}^{pl}$ is error stress and is assumed to be in the form of Eq. (6).

$$\overline{\varepsilon}_f^{pl} = \left[d_1 + d_2 \exp\left(-d_3 \frac{p}{q}\right)\right]\left[1 + d_4 \ln\left(\frac{\dot{\overline{\varepsilon}}^{pl}}{\dot{\overline{\varepsilon}}_0}\right)\right]\left(1 + d_5 \hat{\theta}\right) \tag{6}$$

Where, $d_1 - d_2$ is the material constant to be determined from experiments, p/q three axis tensioning, p pressure stress, q misses equivalent stress. The parameter d_3 is different from the original formula published by *JC*. This difference is explained by the fact that most materials are exposed to a decrease in the value $\overline{\varepsilon}_f{}^{pl}$.

Therefore, usually positive results are obtained from Eq. (6). Friction in the cutting process is affected by *CT*'s, interface between the tool and the chip and the machined surface.

The results will influence tool wear, workpiece surface and generated heat. Therefore, the mathematical model should be able to accurately reflect the highly nonlinear contact between the tool-chip interface and the workpiece. According to Zorev's friction model; tool-chip interface; it has two different contact states: shear zone and contact zone. The friction stress in the shear zone decreases with the chip angle and this friction can be explained by Coulomb's law Eq. (7) [26].

$$\tau_f = \begin{pmatrix} \mu\sigma_n & \mu\sigma_n < the\,slinding\,zone \\ \tau_s & \mu\sigma_n \geq the\,bond\,zone \end{pmatrix} \tag{7}$$

Where; τ_f is the frictional stress at the tool-chip interface, μ friction coefficient, σ_m normal stress at tool-chip interface and τ_s shear stress of the workpiece material. Heat conduction equation, however, is presented in Eq. (8), where a partial differential of 2D heat conduction is taken.

$$\lambda \frac{\partial^2 \theta}{\partial x^2} + \lambda \frac{\partial^2 \theta}{\partial y^2} - \rho C_p \left(\mu_x \frac{\partial \theta}{\partial x} + \mu_y \frac{\partial \theta}{\partial y}\right) + Q = 0 \tag{8}$$

$$Q = \frac{W_h \overline{\varepsilon}\overline{\sigma}}{J} \tag{9}$$

TABLE 4

JC material parameters [28]

A	*B*	*C*	*n*	*m*	*E*	Referance
305	1161	0.01	0.61	0.517	1	Chandrasekaran et al.

Where: λ is the coefficient of thermal conductivity, C specific heat, ρ material density, Q heat production rate per unit volume and X the rate of plastic deformation converted to heat. Where, $W_h = 0.9\overline{\sigma}$ equivalent stress, $\overline{\varepsilon}$ equivalent stress ratio and J is the equivalent coefficient of Joule in Eq. (8) and Eq. (9). TABLE 4 shows the *JC* parameters of stainless steel.

2.5. FEA studies

In the program used to perform the FEA of the machining process, data such as mechanical and thermal values of *CT* and workpiece, cutting parameters, friction type and coefficient, mechanical and thermal boundary conditions of the process must be entered. The closer the parameters entered in the virtual chip removal process is to the experimental conditions, the more the accuracy of the simulation. Fig. 3 shows the boundary conditions required to implement the FEA.

In the numerical model formed, the finite element mesh of the workpiece consists of 3095 triangular elements and 3196 nodes, while the finite element mesh of the tool consists of 1098

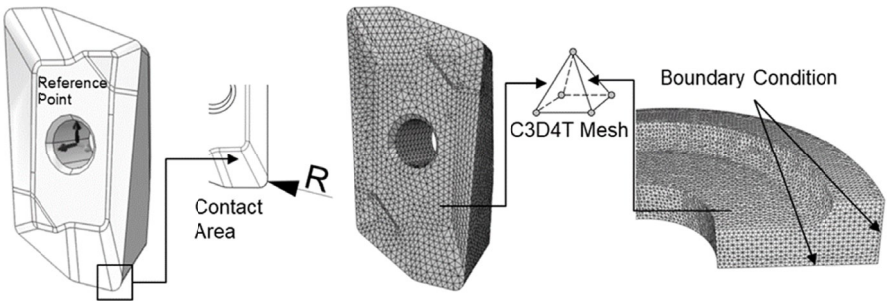

Fig. 3. Boundary conditions and mesh structure of workpiece and *CT* for FEA

triangular elements and 1164 nodes. As the workpiece will be subjected to permanent deformation, it was modelled as plastic, and it was assumed that it exhibited no elastic deformation during the process. When tool wear was not considered, the *CT* was modelled as rigid. On the workpiece, the finite element mesh was formed denser in the regions where the deformation occurred, and coarser in the regions away from the deformation region. The zone containing the dense mesh structure follows the motion of the *CT*. It was limited in the Y and Z axes and the feed in the X axis direction was defined. In addition, the rotary movement along the Z axis was released. The *CT* moves towards the workpiece at a cutting speed of V_c on the X axis, while the *CT* performs the rotational movement.

3. Results and discussion

TABLE 5 shows the S/N ratios calculated by Eq. (1) for the *CT* temperature and cutting forces generated during the milling of Custom 450 stainless steel.

TABLE 5

Test results and S/N ratios based on L16 test design

Exp. No	Control Factors						Experimental Results		*S/N* Ratios	
	A	Cutting Tool (*CT*)	B	Cutting Speed (V_c)	C	Feedrate (*f*)	Temperature (°C)	Cutting Forces – R(*N*)	Temperature (*dB*)	Cutting Forces – R(*dB*)
1	1	T1	1	40	1	0.05	90**	311,2	–39.0849	–49,8608
2	1	T1	2	80	2	0.1	136.89	308,8	–42.7274	–49,7935
3	1	T1	3	120	3	0.15	155.8	306,1	–43.8513	–49,7173
4	1	T1	4	160	4	0.2	226.62	325,5	–47.1060	–50,2510
5	2	T2	1	40	2	0.1	98.01	315,4	–39.8254	–49,9772
6	2	T2	2	80	1	0.05	110.43	287,3**	–40.8617	–49,1667
7	2	T2	3	120	4	0.2	142.37	334,7	–43.0684	–50,4931
8	2	T2	4	160	3	0.15	178.01	315,6	–45.0089	–49,9827
9	3	T3	1	40	3	0.15	105.42	325,7	–40.4585	–50,2564
10	3	T3	2	80	4	0.2	157.69	343,4*	–43.9561	–50,7160
11	3	T3	3	120	1	0.05	188.17	289,1	–45.4910	–49,2210
12	3	T3	4	160	2	0.1	260*	309,5	–48.2995	–49,8132
13	4	T4	1	40	4	0.2	152.02	336,4	–43.6380	–50,5371
14	4	T4	2	80	3	0.15	157.08	330,4	–43.9224	–50,3808
15	4	T4	3	120	2	0.1	168.89	321,2	–44.5521	–50,1355
16	4	T4	4	160	1	0.05	175	296,7	-44.8608	-49,4464

* Max. value; ** Min. value

3.1. Experimental results of tool temperature

Temperatures formed in the cutting zone through milling of Custom 450 stainless steel material with carbide tools was evaluated over the *CT*. The main effect graphs for the *S*/*N* ratios of the control factors on the temperature during the cutting process are shown in Fig. 4. In TABLE 6, the *S*/*N* ratios calculated to determine the optimum cutting conditions for temperature values are given.

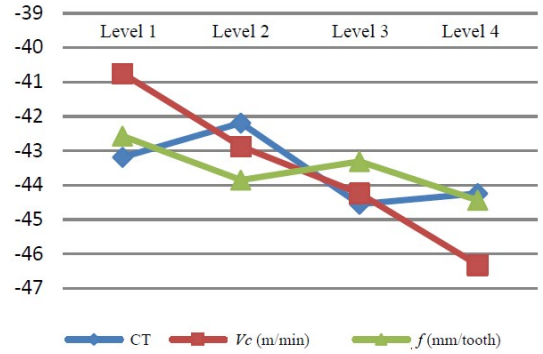

Fig. 4. Main effect graphs for *S*/*N* ratios of temperature values

It is seen that the V_c is the most important control factor affecting the temperature values obtained by milling experiments (Fig. 4) and the difference between *S*/*N* ratios confirms this result (TABLE 6).

TABLE 6

Significance levels of control factors for *S*/*N* ratios of temperature values

Control factors	*S/N* ratios (dB)				Max. Min.	Priority
	Level 1	Level 2	Level 3	Level 4		
CT	–43.19	–42.19	–44.55	–44.24	2.36	2
V_c (m/min)	–40.75	–42.87	–44.24	–46.32	5.57	1
f (mm/tooth)	–42.57	–43.85	–43.31	–44.44	1.87	3

When the TABLE 5 is examined, while the lowest temperature value is measured as 900°C with the T1 coded *CT* at 40 m/min cutting speed and 0.05 mm/tooth feedrate, the highest temperature value is measured as 260°C with the T3 coded *CT* at 160 m/min cutting speed and 0.1 mm/tooth feedrate. The changes in the temperature values resulting from the processing of the Custom 450 material based on the cutting speed-feedrate interaction are shown in Fig. 5. When the graph is examined, while it shows that the temperature increases with the increase in the cutting speed, it also validates the statistical inferences.

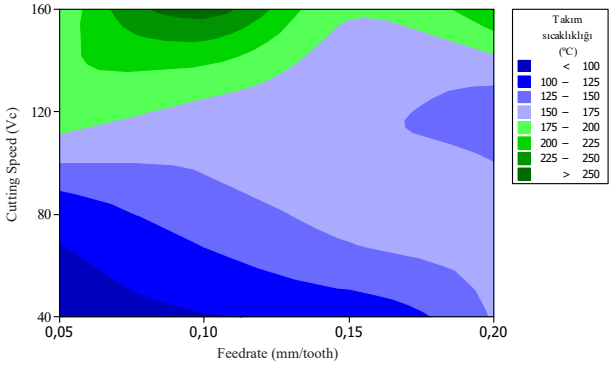

Fig. 5. Effect of cutting speed-feedrate interaction on temperature values

Results of ANOVA applied to temperature values are given in TABLE 7. While the most significant control factor on temperature values is the cutting speed (68.70%), the *CT* (14:45%) is in second place, and the feedrate (7.92%) is in the third place. The conversion of the energy required for plastic deformation to heat, the heat generated by the friction at the tool-chip interface and the heat values coming off with the friction caused by the contact of the *CT* with the newly formed workpiece surface are a result that is expected to increase with the increase in the cutting speed and is in accordance with the literature. *CT* (chip angle, insert radius, coating condition, etc.) is another factor that affects the temperature.

TABLE 7

Results of ANOVA analysis based on *S*/*N* ratios of temperature values

Control Factors	Degree of Freedom (DOF)	Total Square (*CT*)	Average Square (*KO*)	*F*	*P*	Profit (%)
CT	3	13.830	4.610	3.23	0.103	14.45
V_c	3	65.761	21.920	15.38	0.003	68.70
f	3	7.581	2.527	1.77	0.252	7.92
Error	6	8.553	1.425			8.93
Total	15	95.725				100.0
R^2	91.07%					

When Fig. 4 and Fig. 5 are examined, it is seen that the effect of feed rate on temperature is not as effective as cutting speed. However, it is understood that the temperature increases with the increase in the amount of feed. It is expected that about 80% of the heat generated in the cutting zone will go away with the sawdust [29]. This is even more important for the Custom 450 material, which has a low thermal conductivity coefficient. Increasing the feed rate will shorten the milling time [30,31] and therefore the contact time of the hot chip moving away from the cutting area with the cutting tool will be relatively reduced. However, an increase in the feed rate will cause an increase in the chip cross-section, more power requirement, and therefore an increase in the temperature value.

In the Taguchi method, after determining the levels of the control factors that would yield the most appropriate results, verification experiments should be performed in which the accuracy of the optimization is tested. Fig. 4 show that the optimal control factors for tool temperature values are $A_2 - B_1 - C_1$ based on *S*/*N* ratios calculated by the "smallest best" objective function (*CT*: 2, V_c: 40 m/min and *f*: 0.05 mm/tooth).

$$\eta_G = \bar{\eta}_G + \left(\bar{A}_0 - \bar{\eta}_G\right) + \left(\bar{B}_0 - \bar{\eta}_0\right) + \left(\bar{C}_0 - \bar{\eta}_G\right) \tag{9}$$

$$R_{a(hes)} = 10^{-\eta^G/20} \tag{10}$$

The results of the experiment carried out with the levels of optimum control factors are evaluated considering the Confidence Interval (*CI*) calculated in Eq. (11).

$$CI = \sqrt{F_{0,05,(1,\upsilon_e)}\, Ve\, (1/\eta_{eff} + 1/r)} \tag{11}$$

Number of test repetitions η_{eff} is calculated by means of placing the required values of the total number of tests and the sum of the DOF of the control factors, which have a significant effect on the calculation, in Eq. (12).

$$\eta_{eff} = N/1+\upsilon_T \tag{12}$$

$F_{0,05(1.U_e)}$ value is determined from the related Table 7, considering the DOF. Error variance in Eq. (11), is determined with the help of the data in TABLE 7. When the values found were placed in Eq. (11), the *CI* for temperature was calculated to be 4.1318 dB. Comparison of the result of the validation test performed at optimum levels of control factors and the values calculated with the help of Eq. (9) and Eq. (10) is given in TABLE 8. It is seen in Table 8 that the difference between the *S*/*N* ratios of the results from the validation tests and the *S*/*N* ratios of the values calculated using the Eq. (9) and Eq. (10) is –0.1978 dB. When these values are compared, it is seen that the calculated value is smaller than the *CI* value (4.1318 > –0.1978). This result indicates that optimization performed for temperature values is appropriate.

TABLE 8

Comparison of the results of the validation test and the calculated values for temperature values

Material	Validation Experience Results		Calculated Prediction Results		Gap	
	$Temp_{exp.}$ (°C)	*S*/*N* (η_{exp}, dB)	$Temp_{calc.}$ (N)	*S*/*N* ($\eta_{calc.}$, dB)	$Temp_{exp.\ calc.}$	$\eta_{exp\ calc.}$
C450	85.37	–38.626	71.67	–38.428	13.7	–0.197

3.2. Experimental results of cutting forces

The main effect graphs for the *S*/*N* ratios of the cutting forces generated during the milling of the relevant material are given in Fig. 6. In TABLE 9, the calculated *S*/*N* ratios are given in order to determine the optimum cutting conditions for the cutting force values.

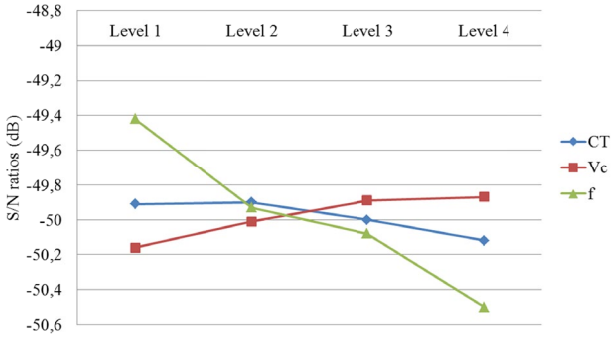

Fig. 6. Main effect plots for *S*/*N* ratios of cutting forces

It is seen that the most important control factor affecting the cutting force values measured as a result of milling experiments

is the feedrate (Fig. 6) and the difference between the *S*/*N* ratios confirms this result (TABLE 9).

TABLE 9

Significance levels of control factors for *S*/*N* ratios of shear force values

Control factors	*S*/*N* ratios (dB)				Max. Min.	Priority
	Level 1	Level 2	Level 3	Level 4		
CT	–49,91	–49,90	–50,00	–50,12	0,22	3
V_c (m/min)	–50,16	–50,01	–49,89	–49,87	0,28	2
f (mm/ thread)	–49,42	–49,93	–50,08	–50,50	1,08	1

When TABLE 5 is examined, the lowest cutting force value is measured as 287.3 N when machining with T2 coded cutting tool at 80 m/min cutting speed and 0.05 mm/tooth feed rate, while the highest cutting force value is measured with T3 coded cutting tool at 80 m/min cutting speed and it was measured as 343.4 N when machining at 0.2 mm/tooth feed. The changes in the cutting force values measured during the machining of the Custom 450 material according to the interaction between cutting speed and feed rate are shown in Fig. 7. When the graph is examined, it is seen that the force values tend to increase with the increase in the amount of progress, and it also confirms the statistical inferences made.

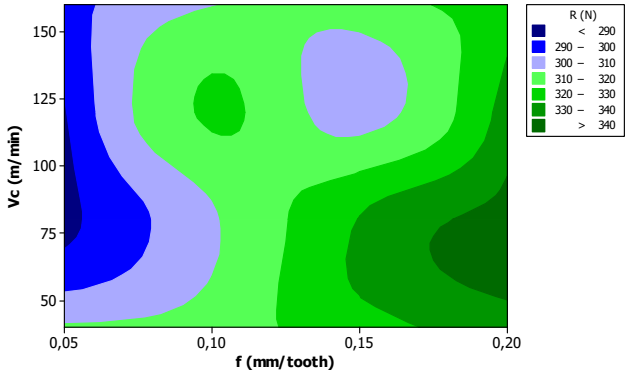

Fig. 7. The effect of cutting speed-feed rate interaction on cutting force values

ANOVA results for shear force values are given in TABLE 10. The most important control factor on the force values is the feed rate (76.2%), while the cutting speed (6.7%) is in the second place and the cutting tool (4.4%) is in the third place. In Fig. 7, it is seen that *R* is significantly affected by the changes in f and V_c. It is seen that there is a significant increase in *R* especially with increasing values off, and a relative decrease in increasing values of V_c (Fig. 6 and Fig. 7). Increasing f will increase the chip cross-sectional area and will require more power in the drilling process [32]. With the increase of V_c, the friction between the cutting tool and the workpiece will increase, thus causing an increase in the heat generated in the cutting zone. The rising heat will reduce the yield strength of the test material somewhat and cause a decrease in the power requirement [32-34]. Moreover, the low thermal conductivity of Custom 450 stainless steel is thought to contribute to this effect. In addition, the fluctuations in the graph are an indication that the cutting tool, which is another control factor, is effective on *R*, although not effectively. The result of the analysis of variance given in TABLE 10 also confirms this determination.

TABLE 10

ANOVA analysis results according to *S*/*N* ratios of shear force values

Control Factors	Degree of Freedom (DOF)	Total Square (CT)	Average Square (KO)	F	P	Profit (%)
CT	3	179,17	59,72	0,69	0,590	4,4
V_c	3	272,49	90,83	1,05	0,436	6,7
f	3	3100,27	1033,42	11,95	0,006	76,2
Error	6	518,80	86,47			12,7
Total	15	4070,74				100.0
R^2	87,26%					

After determining the levels of control factors that will give optimum results, such as the cutting tool temperature, validation experiments should be carried out to test the accuracy of the optimization. The levels of optimum control factors for shear force values according to the *S*/*N* ratios calculated with the "small best" objective function are shown in Fig. 6, where they are A2-B4-C1 (*CT*: 2, V_c: 160 m/min and *f*: 0.05 mm/tooth).

As a result of the necessary calculations (as in temperature calculations), the *CI* value was found to be 25.45. The comparison of the results of the verification test performed at the optimum levels of the control factors and the values calculated with the help of Eq. 9 and Eq. 10 are given in TABLE 11. TABLE 11 shows that the difference between the *S*/*N* ratios of the results obtained from the validation experiments and the *S*/*N* ratios of the values calculated using Eq. 9 and Eq. 10 is –0.4511 dB. When these values are compared, the fact that the calculated value is considerably smaller than the confidence interval value (25.45 > 0.4511) shows that the optimization made is appropriate.

TABLE 11

Comparison of the validation test results for the shear force values with the calculated values

Material	Validation Experience Results		Calculated Prediction Results		Gap	
	R_{exp} (°C)	*S*/*N* (η_{exp}, dB)	$R_{calc.}$ (*N*)	*S*/*N* ($\eta_{calc.}$, dB)	$R_{exp.}$ / $R_{calc.}$	$\eta_{exp.}$ / $\eta_{calc.}$
C450	305,3	–49,6945	289,025	–49,2334	16,275	0,46,11

3.3. FEA results

The finite element analysis was carried out with the optimum cutting conditions obtained as a result of the machining tests made with the samples produced from Custom 450 and the optimization made with the taguchi method and the results were compared. Accordingly, for cutting tool temperature analysis

CT: 2, V_c: 40 m/min and *f*: 0.05 mm/tooth and for cutting force analysis *CT*: 2, V_c: 160 m/min and *f*: 0.05 mm/tooth values were used.

Cutting forces and simulation results obtained from chip removal experiments carried out with samples produced from Custom 450 are shown in Figs 6, 8 and 9 on the same graph comparatively. The graphs show that with increasing cutting speeds and the feedrate, the cutting forces increase. The fact that the cutting forces are increased with the increasing of feedrate is an expected phenomenon in machining [35,36]. This phenomenon is possible to be related with the increased chip cross-section as a result of increased feedrate. Increasing the chip cross-section means that the energy required to remove the chip is increased. Increased energy also causes the axial forces to increase [37,38].

In the experimental study and the results obtained with FEA, the cutting force (Exp.: 256 N, Sim.: 223 N) at 400 rpm and 0.1 mm/min feedrate increased with taking feedrate up to 0.8 mm/min (for F_x: Exp.: 441 N, Sim.: 426 N). Experimental cutting forces were calculated by a dynamometer using DYNOWARE software and by averaging values taken from stationary zones.

Fig. 7 shows the stress and temperature images obtained by FEA. Time-dependent changes of temperature and stresses are presented in the graphs. The obtained results are very close

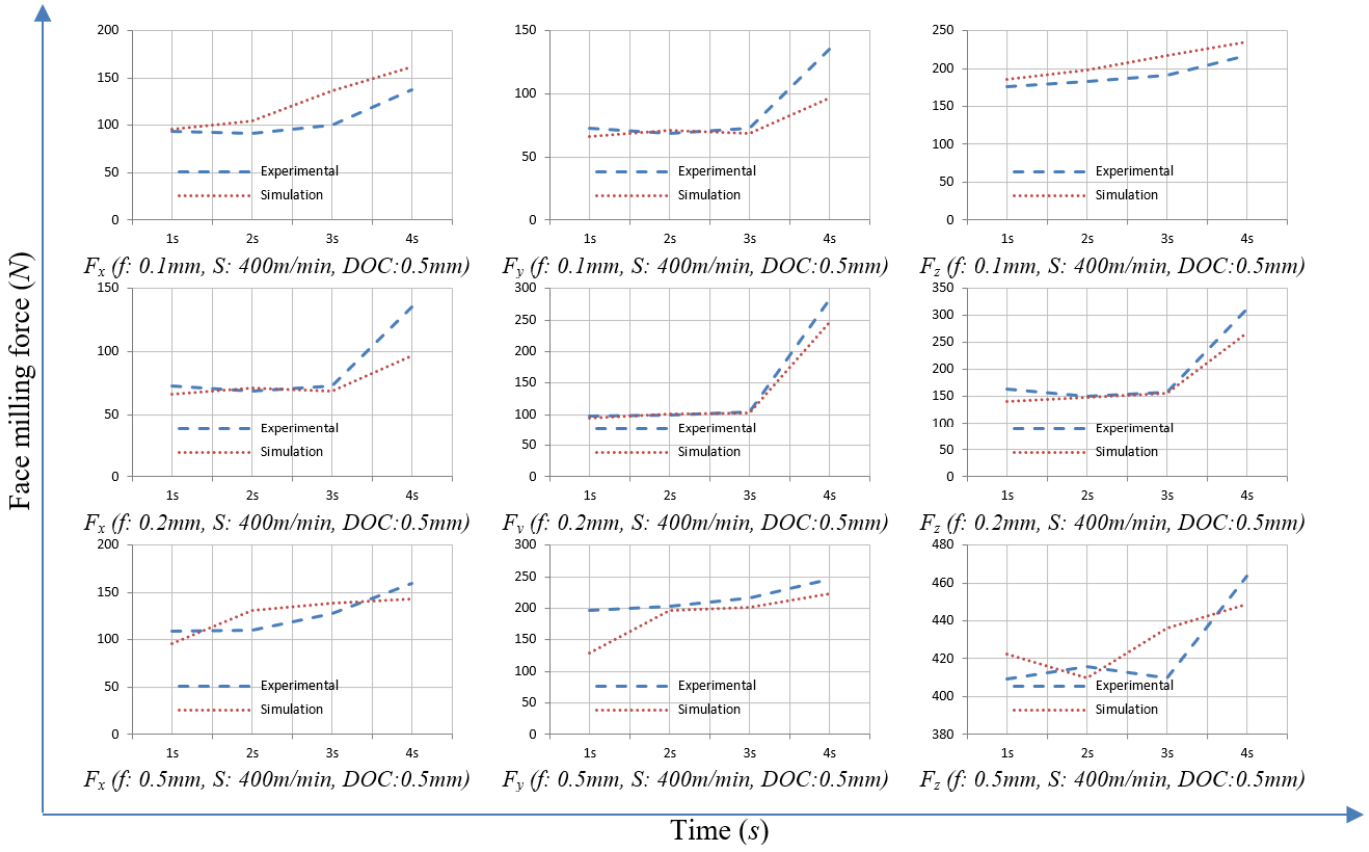

Fig. 8. Comparison of cutting forces measured and simulated in experiments

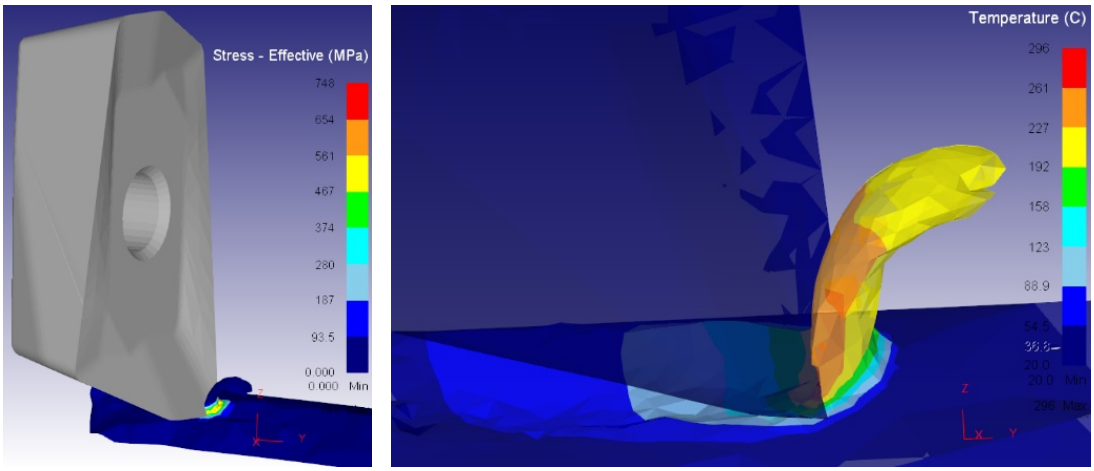

Fig. 9. FEA based simulation results

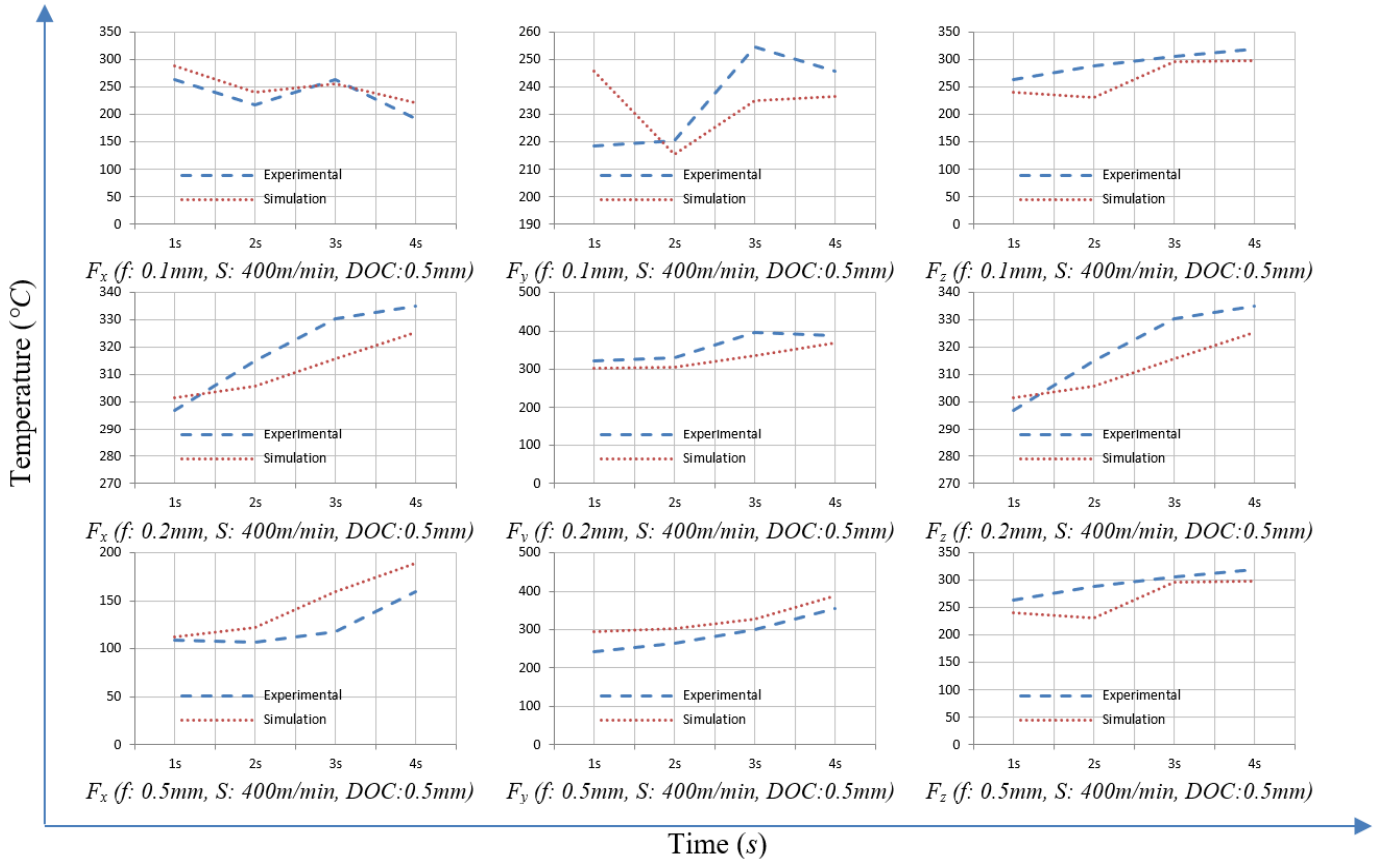

Fig. 10. Comparison of temperature changes measured and simulated in experiments

to the experimental data and the curves obtained by the graphs are consistent with each other. There were 10% differences between the experimental results and the analysis results. The probable reason is assumed to be originated from the fact that the coefficients in the JC parameters entered for the workpiece material model were obtained from the literature and that the actual material model could not be created.

The variation of cutting forces based on the cutting speed and feedrate is given in Figs 6 and 8. When the cutting force graphs obtained are examined, it is observed that the main cutting forces decrease as the cutting rate is increased, in a similar manner in literature and the main cutting forces increase as the feedrate is increased. In simulation models, cutting length is determined to be 5 mm. The reason for the determination of this value as such is the fact that it is the minimum cutting length required for the cutting forces and the resulting temperature to converge in an equilibrium. The cutting forces obtained from the simulations were measured as a mean value at the section where it was stationary (Fig. 7).

As a result of the simulations, the temperatures formed in the tool and workpiece were obtained. The formation of heat on the surface of the rake shown in Fig. 6 is given based on the distance. When the obtained data are examined, it is seen that the region where the temperature increased due to the cutting speed and the high temperature made an effect on the tool surface due to the increasing feedrate expanded. Therefore, it is observed that the temperature spread over a larger area.

4. Conclusions

In this study, the appropriate cutting tool and cutting parameters in the milling of martensitic Custom 450 stainless steel were evaluated in terms of cutting forces and tool temperature, and the results of the experimental study were compared with the finite element method. The following results were obtained:

- While the most important control factor on the average temperature was feedrate with a value of 50.38% and it was the cutting speed on cutting forces with a value of 81.15%.
- As expected, an increase was observed in tool temperature with increased feedrates. The lowest cutting forces values were obtained at the lowest feedrates.
- It is seen that the CT is effective on the tool temperature value. The reason for this is thought to be originating from different coating types and geometries.
- The temperature of the simulation is higher than the experimental results. This is due to the use of a thermal camera. While the thermal camera gives the ambient temperature in the cutting zone, the temperature data on the CT is measured in simulation.
- It was seen that the tool temperature was highly dependent on the cutting speed. With the increased cutting speed, wear on CT was also increased. This is attributed to the fact that an increase in the cutting speed increases the temperature, and this poses a negative impact on the tool life.

REFERENCES

[1] H. Gökçe, Optimisation of cutting tool and cutting parameters in face milling of custom 450 through the taguchi method, Advances in Materials Science and Engineering 2019, 1-10 (2019). DOI: https://doi.org/10.1155/2019/5868132

[2] Y. Turgut, H. Çinici, İ. Şahin, T. Fındık, Study of cutting force and surface roughness in milling of Al/Sic metal matrix composites, Scientific Research and Essays **6** (10), 2056-2062 (2011). DOI: https://doi.org/10.5897/SRE10.496

[3] A. Kulkarni, V. Sargade, C. More, Machinability investigation of AISI 304 austenitic stainless steels using multilayer AlTiN/TiAlN coated carbide inserts, Procedia Manufacturing **20** (1), 548-553 (2018). DOI: https://doi.org/10.1016/j.promfg.2018.02.082

[4] E. Altınkaya, A. Güllü, The effects of tool coating and cutting speed on tool wearing in the machining of stainless steel, Journal of Polytechnic **11** (3), 243-247 (2008). DOI: https://doi.org/10.2339/2008.11.3.243-247

[5] H. Gökçe, M. Yavuz, H. Gökçe, U. Şeker, Verification with finite element methods of drilling performance for original drill geometry, Gazi Journal of Engineering Sciences **3** (1), 27-34 (2017).

[6] H. Gürbüz, U. Şeker, F. Kafkas, Investigation of effects of cutting insert rake face forms on surface integrity, The International Journal of Advanced Manufacturing Technology **90** (9-12), 3507-3522 (2017). DOI: https://doi.org/10.1007/s00170-016-9652-7

[7] İ. Korkut, M. Kasap, İ. Çiftçi, U. Şeker, Determination of optimum cutting parameters during machining of AISI 304 austenitic stainless steel, Materials and Design **25** (4), 303-305 (2004). DOI: https://doi.org/10.1016/j.matdes.2003.10.011

[8] J. Rajaparthiban, A.N. Sait, Experimental investigation on machining of titanium alloy and optimization of its parameters using ann, Mechanics **24** (4), 449-455 (2018). DOI: https://doi.org/10.5755/j01.mech.24.4.20251

[9] E. Budak, Y. Altintas, E.J. Armarego, Prediction of milling force coefficients from orthogonal cutting data, Journal of Manufacturing Science and Engineering **118** (2), 216-224 (1996). DOI: https://doi.org/10.1115/1.2831014

[10] E. Kuram, Effects of different coating materials on tool wear, cutting forces and surface roughness in milling of AISI 304, Journal of Polytechnic **19** (4), 433-443 (2016).

[11] G. Uzun, İ. Korkut, The effects of cutting conditions on the cutting torque and tool life in the tapping process for AISI 304 stainless steel, Materials and Technology **50** (2), 275-280 (2016). DOI: https://doi.org/10.17222/mit.2015.044

[12] Y. Fedai, A. Unuvar, H.K. Akın, G. Başar, ANFIS modeling of surface roughness in milling operation of 316L stainless steels, Düzce University Journal of Science and Technology **7** (1), 98-110 (2019).

[13] W. Zhang, X. Wang, Y. Hu, S. Wang, Predictive modelling of microstructure changes, micro hardness and residual stress in machining of 304 austenitic stainless steel, International Journal of Machine Tools and Manufacture **130-131** (1), 36-48 (2018). DOI: https://doi.org/10.1016/j.ijmachtools.2018.03.008

[14] R. Shashanka, O. Uzun, D. ChairaCakan, Synthesis of nanostructured duplex and ferritic stainless steel powders by dry milling andits comparison with wet milling, Archives of Metallurgy and Materials **65** (1), 5-14 (2020). DOI: https://doi.org/10.24425/amm.2019.131091

[15] H. Gökçe, İ. Çiftçi, H. Demir, Cutting parameter optimization in shoulder milling of commercially pure molybdenum, Journal of the Brazilian Society of Mechanical Sciences and Engineering **40** (360), 1-11 (2018). DOI: https://doi.org/10.1007/s40430-018-1280-8

[16] G. Basmacı, Optimization of processing parameters of AISI 316-Ti stainless steels, Academic Platform Journal of Engineering and Science **6** (3), 1-7 (2018).

[17] A. Selaimia, M.A. Yallese, H. Bensouilah, I. Meddour, R. Khattabi, T. Mabrouki, Modeling and optimization in dry face milling of X2CrNi18-9 austenitic stainless steel using RMS and desirability approach, Measurements **107** (1), 53-67 (2017). DOI: https://doi.org/10.1016/j.measurement.2017.05.012

[18] V. Varghese, D. Chakradhar, M.R. Ramesh, Micro mechanical characterization and wear performance of TiAlN/NbN PVD coated carbide inserts during end milling of AISI 304 austenitic stainless steel, Materials Today: Proceedings **5** (1), 12855-12862 (2018). DOI: https://doi.org/10.1016/j.matpr.2018.02.270

[19] E. Kuram, B. Özçelik, Micro milling performance of AISI 304 stainless steel using taguchi method and fuzzy logic modelling, Journal of Intellectual Manufacturing **27** (1), 817-830 (2016). DOI: https://doi.org/10.1007/s10845-014-0916-5

[20] T.R. Lin, Optimization technique for face milling stainless steel with multiple performance characteristics, International Journal of Advanced Manufacturing Technology **19** (1), 330-335 (2002). DOI: https://doi.org/10.1007/s001700200021

[21] T.R. Lin, Experimental study of burr formation and tool chipping in the face milling of stainless steel, Journal of Materials Processing Technology, **108** (1), 12-20 (2000). DOI: https://doi.org/10.1016/s0924-0136(00)00573-2

[22] M. Nordin, R. Sundstrom, T. I. Selinder, and S. Hogmark, Wear and failure mechanisms of multilayered PVD TiN/TaN coated tools when milling austenitic stainless steel, Surface and Coatings Technology **133-134**, 240-246, (2000).

[23] A. Qasim, S. Nisar, A. Shah, M.S. Khalid, M.A. Sheikh, Optimization of process parameters for machining of AISI 1045 steel using taguchi design and anova, Simulation Modelling Practice and Theory **59** (1), 36-51 (2015). DOI: https://doi.org/10.1016/j.simpat.2015.08.004

[24] A.M. Pantel, M. Fontaine, G. Michel, S. Thibaud, J.C. Gelin, Experimental Investigations from Conventional to High-Speed Milling on a 304L Stainless Steel, International Journal of Advanced Manufacturing Technology **69** (1), 2191-2213 (2013). DOI: https://doi.org/10.1007/s00170-013-5159-7

[25] https://www.ulbrich.com/uploads/data-sheets/Custom-450-Stainless steel-UNS-s45000.pdf.

[26] H. Gökçe, Prediction of nonlinear dynamic impact force history by finite element method, Journal of Engineering Science and Technology Review **11** (2), 32-37 (2018). DOI: https://doi.org/10.25103/jestr.113.07

[27] M. Storchak, P. Rupp, H.C. Möhring, T. Stehle, Determination of Johnson-Cook constitutive parameters for cutting simulations, Metals **9** (473), 1-17 (2019). DOI: https://doi.org/10.3390/met9040473

[28] R. Chandrasekaran, H. Chazal, Modeling of Material Flow Stress in Chip Formation Process from Orthogonal Milling and Split Hopkinson Bar Test, Machine Science and Technology **9** (1), 131-145 (2005). DOI: https://doi.org/10.1081/MST-200051380

[29] M. Günay, T. Meral, Modelling and multiresponse optimization for minimizing burr height, thrust force and surface roughness in drilling of ferritic stainless steel, Indian Academy of Sciences **45**, 275 (2020). DOI: https://doi.org/10.1007/s12046-020-01490-3.

[30] T. Meral, M. Günay, Modelling and optimization of burr height in fiber laser drilling of ferritic stainless steel, Manufacturing Technologies and Applications **1** (2), 32-39 (2020).

[31] A. Mavi, Gri ilişkisel analiz yöntemi ile dubleks paslanmaz çeliklerin delinmesinde yüzey form özelliklerini etkileyen optimum kesme parametrelerinin belirlenmesi, Gazi University Journal of Science Part C: Design and Technology **6**, 634-643 (2018).

[32] E. Ekici, A.R. Motorcu, G. Uzun, An investigation of the effects of cutting parameters and graphite reinforcement on quality characteristics during the drilling of Al/10B4C composites, Measurement **95**, 395-404 (2017).

[33] G. Uzun, U. Gökmen, H. Çinici, M. Türker, Effect of cutting parameters on the drilling of AISI7 metallic foams", Materials and Technology **51** (1), 19-24 (2017).

[34] İ. Çitci, H. Gökçe, Optimisation of cutting tool and cutting parameters in machining of molybdenum alloys through the Taguchi Method, Journal of the Faculty of Engineering and Architecture of Gazi University **34**, 1, 201-213 (2019). DOI: https://doi.org/10.17341/gazimmfd.416482

[35] A. Yıldız, A. Kurt, A., S. Yağmur, Finite element simulation of drilling operation and theoretical analysis of drill stresses with the deform-3D, Simulation Modelling Practice and Theory, 104, (2020).

[36] A. Attanasioa, F. Fainia, J.C. Outeirob, FEM Simulation of Tool Wear in Drilling, Procedia CIRP **58**, 440-444 (2017).

[37] U.M.R. Paturi, S.K.N. Narala, R.S. Pundir, Constitutive flow stress formulation, model validation and FE cutting simulation for AA7075-T6 aluminum alloy, Materials Science and Engineering: A **605**, 176-185 (2014).

[38] A. Majeed, A. Iqbal, J. Lv, Enhancement of tool life in drilling of hardened AISI 4340 steel using 3D FEM modeling, The International Journal of Advanced Manufacturing Technology **95**, 1875-1889 (2018).